

Neoproterozoic sand wedges: crack formation in frozen soils under diurnal forcing during a snowball Earth

Adam C. Maloof^{a,*}, James B. Kellogg^a, Alison M. Anders^b

^a Department of Earth and Planetary Sciences, Harvard University, 20 Oxford Street, Cambridge, MA 02138, USA

^b Department of Geological Sciences, University of Washington, Seattle, WA 98195, USA

Received 2 May 2002; received in revised form 16 September 2002; accepted 16 September 2002

Abstract

Thermal contraction cracking of permafrost produced sand-wedge polygons at sea level on the paleo-equator during late Neoproterozoic glacial episodes. These sand wedges have been used as evidence for high ($\geq 54^\circ$) paleo-obliquity of the Earth's ecliptic, because cracks that form wedges are hypothesized to require deep seasonal cooling so the depth of the stressed layer in the ground reaches ≥ 1 m, similar to the measured depths of cracks that form wedges. To test the counter hypothesis that equatorial cracks opened under a climate characterized by a strong diurnal cycle and low mean annual temperature (snowball Earth conditions), we examine crack formation in frozen ground subject to periodic temperature variations. We derive analytical expressions relating the Newtonian viscosity to the potential crack depth, concluding that cracks will form only in frozen soils with viscosities greater than $\sim 10^{14}$ Pa s. We also show numerical calculations of crack growth in frozen soils with stress- and temperature-dependent rheologies and find that fractures may propagate to depths 3–25 times the depth of the thermally stressed layer in equatorial permafrost during a snowball Earth because the mean annual temperature is low enough to keep the ground cold and brittle to relatively great depths.

© 2002 Elsevier Science B.V. All rights reserved.

Keywords: ice wedges; snowball Earth; obliquity of the ecliptic; Neoproterozoic; periglacial features; permafrost; paleoclimatology; Mars

1. Introduction

The presence of sand-wedge polygons at the paleo-equator led Williams [1–3] to suggest that a higher obliquity of the Earth's ecliptic relative

to the plane of the solar system ($\geq 54^\circ$ as compared to $23.25 \pm 1.25^\circ$ today) was required in the Neoproterozoic both to drop mean annual temperature below 0°C and to increase seasonality at the paleo-equator. The snowball Earth hypothesis [4–6] was proposed as an alternative to high Earth obliquity in an attempt to explain the association of distinctive cap carbonate rocks [7–10] with low-latitude glacial deposits. We use analytical and numerical models of tensile stress and potential

* Corresponding author. Tel.: +1-617-495-0367;
Fax: +1-617-496-0434.
E-mail address: maloof@fas.harvard.edu (A.C. Maloof).

crack growth in frozen soil to test the hypothesis that fractures which form sand wedges might have occurred at the equator under snowball Earth climate conditions.

1.1. Modern sand wedges

On Earth and Mars today, polygonal fracture networks caused by thermal contraction cracking of frozen ground are found poleward of 17° latitude [11–16]. At high latitudes on Earth, sand/ice wedges are thought to form by the following general process. First, when autumn begins, the 0.5–4 m thick active (seasonally frozen and thawed) layer developed during the summer melt season begins to freeze. Next, when over the course of 24–96 h the first major winter cold front passes through, the already frozen ground contracts and cracks form [17]. The cracks propagate to the same depth that the cold wave penetrates, as ground beneath this stressed layer remains relatively warm and thermal stresses are easily dissipated by viscous processes. The deepest cracks form in mid-winter, when most or all of the active layer is refrozen and the soil column becomes continuously brittle to 10–1000 m depth, but snowcover is not too thick to insulate the ground from cold waves at the surface [18]. Wind-blown sand/snow, segregation ice, or spring meltwater fills the crack. Wedges tend to grow in subsequent years because the sand or ice filling the wedge has a lower tensile strength than the heterogeneous permafrost around it, causing new cracks to exploit existing wedges. However, in any given year, only 8–75% of the existing sand/ice wedges crack again and grow [18–20].

Although diurnal temperature variations may be very large (10–30°C) in tropical deserts, the cold wave is brief (<12 h) and only penetrates 17 cm into the relatively warm ground. Today, only very shallow thermal contraction cracks result from daily temperature fluctuations, even in the high-altitude periglacial environment of Mount Kilimanjaro [21]. No Martian sand wedges have been noted equatorward of 17° , although their development is considered possible by Mellon [22], and the presence of equatorial ground ice has been suggested by Lanagan et al. [23].

1.2. Neoproterozoic sand wedges

Sand-wedge polygons related to thermal contraction cracking of permafrost are reported from Neoproterozoic successions in Australia [24], Mauritania [25], Spitsbergen [26], Northern Norway [27], Southern Norway [28], and Scotland [29]. All of these sand wedges likely developed at or near sea level, and the wedges of South Australia are constrained by reliable paleomagnetic data to have formed at 7_{-7}^{+6} degrees latitude [30–32]. The wedges were filled with sand, commonly laminated vertically or parallel to crack margins, and most of the wedges were developed in sand or diamicton.

1.3. Snowball Earth conditions

During a snowball Earth, mean daily temperatures at the equator would be below 0°C and the air would be extremely dry [33]. On summer days, when minor melting occurred at the ground surface, soil temperatures would not rise above 0°C until all of the ground ice was melted [34]. Whatever meltwater might be generated during a summer day would either completely refreeze at night or evaporate away. The presence of sand wedges rather than ice wedges supports the latter hypothesis, in which the upper soil was very dry and thermal contraction cracks were never filled with meltwater. Because summer ground temperatures did not exceed 0°C and liquid water was transient, permafrost remained extremely brittle throughout the year. In the winter, cracks initiated in the upper 16 cm of permafrost may have propagated to depths on the order of 1 m due to the concentration of stresses at fracture tips and the relatively easy fracture of brittle materials.

We develop a model of pre-fracture stress accumulation and the resulting potential fracture depth in permafrost to investigate the hypothesis that large stresses associated with the diurnal temperature cycle during a snowball Earth could have been responsible for sand-wedge growth at the equator. We drive the system with air temperatures that vary sinusoidally at the ground surface with amplitude of 10–25 K about a mean of 243–253 K over a period of 21.9 ± 0.4 h [35,36]. For

reference, low-latitude terrestrial deserts commonly experience diurnal temperature variations of 30 K [37] and the mean annual temperature at sea level in the Dry Valleys, McMurdo Sound, Antarctica is 253 K.

2. The model

2.1. Temperature

We are concerned with periodic temperature variations of the form:

$$T(z=0, t) = \Delta T \sin(\omega t) \quad (1)$$

where T is the temperature, ΔT is the amplitude of the temperature variation at the surface, ω is the angular frequency of the variation, and t is the time. Temperature as a function of depth is (e.g. [38]):

$$T(z, t) = \Delta T e^{-z'} \sin(\omega t - z') \quad (2)$$

where z' is the dimensionless depth, normalized to the depth of penetration of the temperature variations (the ‘skin depth’):

$$z_\omega = \sqrt{\frac{2\kappa}{\omega}} \quad (3)$$

and κ is the thermal diffusivity. Note that $z' = z/z_\omega$ is a phase lag associated with conduction of the surface temperature signal to finite depths.

The time derivative of temperature is then:

$$\dot{T}(z, t) = \Delta T e^{-z'} \omega \cos(\omega t - z') \quad (4)$$

2.2. Stress and strain rate

We follow Mellon [22] in treating frozen soil as a Maxwell fluid, i.e. a spring and dashpot in series, representing the elastic and viscous components of strain, ϵ_{ij}^e and ϵ_{ij}^η , respectively (Fig. 1). In addition (like Mellon), we add a component of strain due to the thermal expansion and contraction, ϵ_{ij}^T . Differentiating with respect to time, we

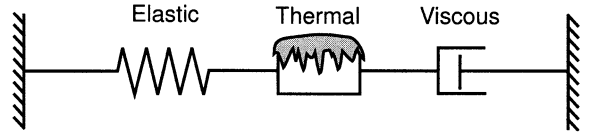


Fig. 1. Thermal stresses applied to a spring and dashpot in series, after Mellon [22]. See Eq. 5.

arrive at an expression for the total strain rate $\dot{\epsilon}_{ij}$:

$$\dot{\epsilon}_{ij} = \dot{\epsilon}_{ij}^e + \dot{\epsilon}_{ij}^T + \dot{\epsilon}_{ij}^\eta \quad (5)$$

Because the elastic response is instantaneous, the elastic strain rate is related simply to the rate of change of applied stress $\dot{\sigma}_{ij}$:

$$\dot{\epsilon}_{ij}^e = \frac{1+\nu}{E} \dot{\sigma}_{ij} - \frac{\nu}{E} \dot{\sigma}_{kk} \delta_{ij} \quad (6)$$

where E is Young’s modulus, ν is Poisson’s ratio, and δ_{ij} is the Kronecker delta. We have neglected higher-order terms involving the temperature derivatives of material properties because they are not significant.

The viscous strain rate is a complicated function of temperature and stress. However, understanding the creep behavior of frozen ground is critical for determining whether thermal stress will be relaxed viscously or will lead to cracking. In Section 3, we study the behavior of the model analytically, assuming a linear relationship between stress and strain rate. In Section 4, we develop a theoretical model for the effective viscosity of frozen ground under cyclic loading and apply it to the results of Section 3. And in Section 5, we perform a numerical integration of the model using non-linear viscosity laws. For now, we employ a general power-law rheology that can be described by the Weertman equation:

$$\dot{\epsilon}_{ij}^\eta = \text{sign}(s_{ij}) A_0 e^{-Q/RT} |s_{ij}|^n \quad (7)$$

where A_0 is a constant related to the viscosity of the material, Q is the activation energy, R is the Rydberg gas constant, T is the absolute temperature, n is of order one, and $s_{ij} = \sigma_{ij} - (1/3)\sigma_{kk}$ is the deviatoric stress. Note that we have been careful to define the sign of the viscosity term such that it always acts to relieve the deviatoric stress.

The thermal strain rate is related to the rate of change of temperature, \dot{T} , through the thermal expansivity, α , according to:

$$\dot{\epsilon}_{ij}^T = \alpha \dot{T} \delta_{ij} \quad (8)$$

where we have adopted the convention that tensile stresses and strains are positive.

Combining these terms, we find that:

$$\dot{\epsilon}_{ij} = \frac{1+\nu}{E} \dot{\sigma}_{ij} - \frac{\nu}{E} \dot{\sigma}_{kk} \delta_{ij} + \text{sign}(s_{ij}) A_0 e^{-Q/RT} |s_{ij}|^n + \alpha \dot{T} \delta_{ij} \quad (9)$$

As discussed by Mellon [22], if we assume horizontal isotropy of material properties, the horizontal stresses are equal in all directions ($\sigma_{11} = \sigma_{22} = \sigma$), and the total horizontal strain rate $\epsilon = \epsilon_{11} = \epsilon_{22}$ must vanish. Therefore, the horizontal components of Eq. 9 reduce to:

$$\dot{\sigma} = E^* \left[-\text{sign}(\sigma) A_0 e^{-Q/RT} \left| \frac{\sigma}{2} \right|^n - \alpha \dot{T} \right] \quad (10)$$

where

$$E^* = \frac{E}{1-\nu} \quad (11)$$

The factor of 1/2 in the power-law stress term is introduced for consistency with experiment; laboratory creep experiments generally derive the material properties under uniaxial or triaxial stress, whereas we are concerned with conditions of plane stress with $\sigma_{33} = 0$ [22].

2.3. Crack propagation

The stress field of a linear elastic half-space is changed drastically by the presence of an isolated, sharp crack. Assuming the walls of such a crack to be stress-free, we can derive expressions for the net stress in the solid (e.g. [39,40]). The presence of the crack focuses tensile stresses around the crack tip, actually leading to a stress singularity at the tip itself (this is clearly unphysical, as plasticity in the crack tip region negates the assumption of linear elasticity locally). Extension of the crack releases the accumulated elastic strain en-

ergy; the classical Griffith energetic approach seeks to balance this strain energy release rate against a fracture resistance term owing to changes in surface free energies and dissipative effects.

An equivalent treatment involves the use of a crack edge intensity factor, K , which is a function of the applied stress geometry and magnitude as well as the material properties of the elastic medium. The solution for an arbitrary symmetric horizontal stress field $\sigma(z)$ is (e.g. [40]):

$$K = \frac{2\psi\sqrt{b}}{\pi} \int_0^b \frac{\sigma(z)}{\sqrt{b^2-z^2}} dz \quad (12)$$

where ψ is a geometric correction factor. For straight edge cracks in a semi-infinite medium, $\psi \approx 1.12\sqrt{\pi}$.

Lachenbruch [39] found analytical solutions to Eq. 12 for two simple loading geometries. The first is the crack stress intensity factor owing to a tensile, horizontal stress $\bar{\sigma}$ applied uniformly from the surface ($z=0$) to a depth, a , less than the crack depth, b . In that case:

$$K_{\bar{\sigma}} = \frac{2\psi}{\pi} \bar{\sigma} \sqrt{b} \sin^{-1} \left(\frac{a}{b} \right) \quad (13)$$

The second result of Lachenbruch that we apply here is for a stress that is linearly increasing with depth. Specifically, the contribution to the crack edge stress intensity factor from gravity is given by:

$$K_{\rho} = -\frac{2\psi}{\pi} \rho g b^{3/2} \quad (14)$$

where ρ is the density of the medium and g is the gravitational acceleration. For the depth range we consider below (≤ 3 m), K_{ρ} is small (≤ 0.17 MPa m^{1/2}), and we will neglect its contribution in the analytical treatment that follows (see Fig. 2).

3. Analytical solutions

Because of the potential non-linearity of the stress-strain rate relationship, we cannot solve Eq. 10 analytically. However, if we linearize the

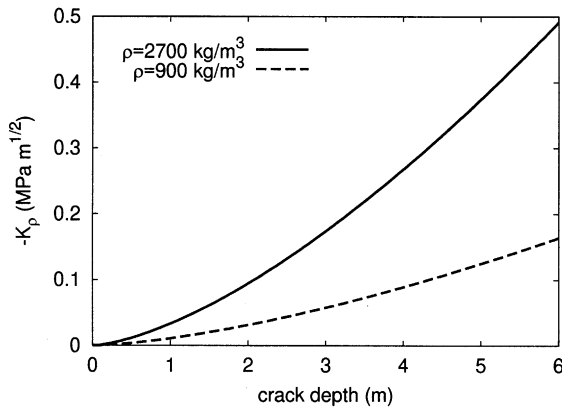


Fig. 2. The contribution to the stress intensity factor from gravity for pure sand ($\rho=2700 \text{ kg m}^{-3}$) and pure ice ($\rho=900 \text{ kg m}^{-3}$). See Eq. 14.

viscosity, we can explore the basic behavior of the system and identify the most critical parameters. We argue below that this is a reasonable approximation that may, in fact, come very close to reality. We proceed by defining an effective linear viscosity η :

$$\eta = \frac{1}{A_0} e^{Q/RT} 2^n \bar{\sigma}^{1-n} \quad (15)$$

where \bar{T} is a representative temperature and $\bar{\sigma}$ is a representative stress. This stress should not be more than the yield stress of the material ($\sim 0.5\text{--}2 \text{ MPa}$ for ice) as these stresses are never actually realized within the material. Note that the values of A_0 , Q , and n will vary depending on which creep mechanism is dominant in the material under a set of stress, strain, strain rate, and temperature conditions [41]. In Section 4.1, we discuss specific creep mechanisms and attempt to define an appropriate effective viscosity for frozen ground.

3.1. Stress

With this simplified viscosity law, we can rewrite Eq. 10 as:

$$\dot{\sigma} = E^* \left(-\frac{\sigma}{\eta} \alpha \dot{T} \right) \quad (16)$$

Substituting Eq. 4 and rearranging, we find:

$$\dot{\sigma} + \frac{1}{\tau_\sigma} \sigma = \sigma_\theta e^{-z'} \omega \cos(\omega t - z') \quad (17)$$

where the stress relaxation time (or Maxwell time) τ_σ is:

$$\tau_\sigma = \frac{\eta}{E^*} \quad (18)$$

and the maximum thermal stress at the surface is:

$$\sigma_\theta = E^* \alpha \Delta T \quad (19)$$

Eq. 17 has the solution:

$$\sigma = \sigma_0 e^{-t/\tau_\sigma} - \sigma_\theta e^{-z'} \frac{\omega \tau_\sigma}{1 + \omega^2 \tau_\sigma^2} [\cos(\omega t - z') + \omega \tau_\sigma \sin(\omega t - z')] \quad (20)$$

where σ_0 is the stress at time $t=0$. This solution has the standard form of a visco-elastic solid under harmonic stress (e.g. [42]). The first term on the right is simply a viscous relaxation from the initial state of stress. The periodic terms are more interesting. The in-phase term represents the instantaneous elastic response of the material, whereas the out-of-phase term reflects the viscous response.

We note that the dimensionless frequency $\omega \tau_\sigma$ indicates the relative importance of the viscous and elastic terms. If $\omega \tau_\sigma \ll 1$, then the viscous term dominates, and non-transient stresses are very small. On the other hand, if $\omega \tau_\sigma \gg 1$, then the behavior is essentially elastic and stresses may be large.

We will see below that calculated stresses may exceed the tensile strength of permafrost. Thus, the application of this model may involve stresses that are unrealistically high. We will set aside this complication for now and show in Section 6 that this simplification does not lead to a gross over-prediction of crack depth.

3.2. Crack edge stress intensity factor

We can now substitute our expression for stress

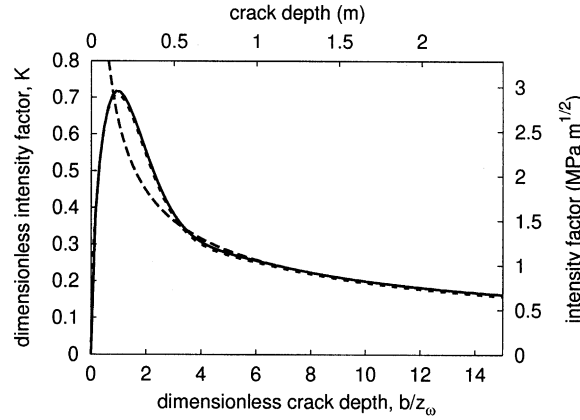


Fig. 3. Crack-edge stress intensity factor as a function of crack depth. The solid curve is derived from a numerical integration of Eq. 21, whereas the dashed curve is the large b approximation of Eq. 26. The dotted curve (largely overlapping the solid curve) shows the results of a full numerical solution, as discussed in Section 5. To dimensionalize the vertical scale, we multiply by $\sigma_{\theta} \sqrt{z_{\omega}} \gamma(\omega \tau_{\sigma})$. Notice that K is initially zero at the surface because there is no crack length yet developed to concentrate stresses at the crack tip. K increases rapidly with depth until K reaches a maximum near the skin depth ($b/z_{\omega} \approx 1$), and then decreases with depth as applied tensile stresses near the crack tip approach zero.

as a function of depth into Eq. 12 to find:

$$K_{\theta} = -\frac{2\psi}{\pi} \sqrt{b} \sigma_{\theta} \frac{\omega \tau_{\sigma}}{1 + \omega^2 \tau_{\sigma}^2} \int_0^b \frac{e^{-z'} [\cos(\omega t - z') + \omega \tau_{\sigma} \sin(\omega t - z')]}{\sqrt{b^2 - z'^2}} dz' \quad (21)$$

This integral has no analytical solution but can be integrated numerically, as shown in Fig. 3 for $t = t_{\max}$, as defined below. In addition, we can solve for the end-member case $b \gg z_{\omega}$ to find:

$$K_{\theta} \approx \frac{\psi}{\pi} \sigma_{\theta} \left\{ \frac{\omega \tau_{\sigma}}{1 + \omega^2 \tau_{\sigma}^2} \left[(1 + \omega \tau_{\sigma}) \sin(\omega t) + (1 - \omega \tau_{\sigma}) \cos(\omega t) \right] \right\} \quad (22)$$

Since we are only concerned with the maximum value of K_{θ} as a function of depth, we can maximize the term in the curly brackets with respect to time. We find that it is maximized at a time t_{\max} , where:

$$t_{\max} = \frac{1}{\omega} \arctan \left(\frac{1 + \omega \tau_{\sigma}}{1 - \omega \tau_{\sigma}} \right) \quad (23)$$

We then define a weighting function:

$$\gamma(\omega \tau_{\sigma}) = \frac{\omega \tau_{\sigma}}{1 + \omega^2 \tau_{\sigma}^2} \left[(1 + \omega \tau_{\sigma}) \sin(\omega t_{\max}) + (1 - \omega \tau_{\sigma}) \cos(\omega t_{\max}) \right] \quad (24)$$

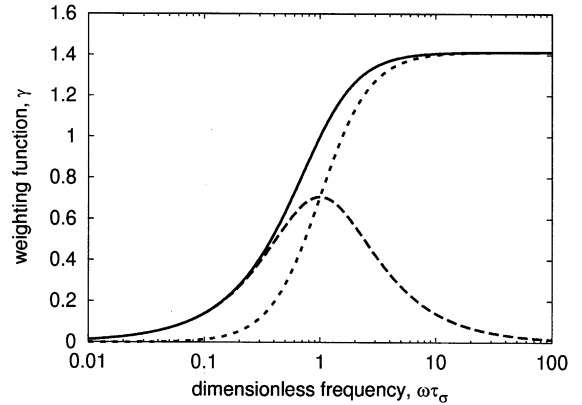


Fig. 4. Weighting function vs. dimensionless frequency. The dotted and dashed curves represent the maximum amplitude of the contribution to the weighting function by the in-phase and out-of-phase stresses, respectively (see Eq. 20). The latter has the form of the Debye relaxation peak. The solid curve shows the combined maximum (see Eq. 25); it is not simply the sum of the other two terms, as the cosine and sine terms cannot simultaneously contribute their maximum amplitudes.

which simplifies to:

$$\gamma(\omega\tau_\sigma) = \frac{\omega\tau_\sigma\sqrt{2}}{\sqrt{1 + \omega^2\tau_\sigma^2}} \quad (25)$$

The behavior of this function is shown in Fig. 4. The maximum value of K_θ , then, can be written as:

$$K_\theta^{max} \approx \frac{\Psi}{\pi} \frac{z_\omega}{\sqrt{b}} \sigma_\theta \gamma(\omega\tau_\sigma) \quad (26)$$

We show this approximation along with the full solution in Fig. 3. In general, we will be concerned with crack depths significantly greater than the thermal penetration depth, z_ω , so the approximation of Eq. 26 will be appropriate.

3.3. Crack depth

In a simplified view of fracture mechanics, a crack will propagate as long as the crack edge stress intensity factor exceeds some critical value, K_c , which expresses the ‘toughness’ of the material. Neglecting the contribution of overburden, K_ρ (Fig. 2), the maximum depth of crack propagation, b_{max} , can be found from Eq. 26 by substituting K_c for K_θ and rearranging to find:

$$b_{max} \approx \left[\frac{\Psi}{\pi} \frac{\sigma_\theta z_\omega}{K_c} \gamma(\omega\tau_\sigma) \right]^2 \quad (27)$$

Again, it is instructive to examine the end-member behavior of this equation. At high dimensionless frequencies ($\omega\tau_\sigma \gg 1$), the material is effectively elastic, and Eq. 27 simplifies to:

$$b_{max} \approx b^e = \frac{\kappa}{\omega} \left[\frac{2\Psi}{\pi} \frac{\alpha\Delta T}{K_c} \frac{E}{1-\nu} \right]^2 \quad (28)$$

If $\omega\tau_\sigma \ll 1$, the material is effectively viscous, and:

$$b_{max} \approx b^\eta = \kappa \omega \left[\frac{2\Psi}{\pi} \frac{\alpha\Delta T \eta}{K_c} \right]^2 \quad (29)$$

The transition between these two cases occurs when $\omega\tau_\sigma \sim 1$. For both ice and rock, $\kappa \approx 10^{-6} \text{ m}^2 \text{ s}^{-1}$. If we are concerned with diurnal forcing

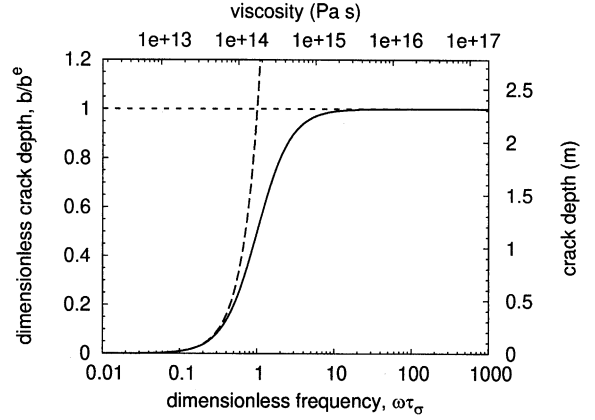


Fig. 5. Potential crack depth, b , as a function of frequency, $\omega\tau_\sigma$ assuming no overburden (see Eq. 27). The primary axes correspond to dimensionless quantities. The secondary axes are dimensional, assuming $\kappa = 10^{-6} \text{ m}^2 \text{ s}^{-1}$, $\omega(600 \text{ Ma}) = 7.97 \times 10^{-5} \text{ s}^{-1}$, $\Delta T = 20 \text{ K}$, $T_{avg} = 243 \text{ K}$, $E = 10 \text{ GPa}$, $\nu = 0.3$, $\alpha = 2.3 \times 10^{-5} \text{ K}^{-1}$, $K_{IC} = 0.6 \text{ MPa}$. The solid curve represents the full potential crack depth, whereas the dashed and dotted curves show the viscous and elastic approximations, respectively.

on Earth 600 Ma, $\omega = 7.97 \times 10^{-5} \text{ s}^{-1}$ [35,36]. Young’s modulus, E , and Poisson’s ratio, ν , are approximately 10 GPa and 0.3, respectively (Section 4.2). Therefore, the transition from viscous to elastic behavior occurs when:

$$\eta = \eta_c = \frac{1}{\omega} \frac{E}{1-\nu} \approx 1.8 \times 10^{14} \text{ Pa s} \quad (30)$$

These relationships are plotted in Fig. 5. The figure shows that the details of the viscosity are not likely to be important; if we can constrain the effective viscosity to be greater than $1.8 \times 10^{14} \text{ Pa s}$, we will potentially have significant cracking. Otherwise, no cracking will develop that is attributable to this mechanism.

4. Material parameters

4.1. Effective viscosity

As shown above, the viscous behavior of permafrost critically affects the potential for crack formation. Despite its complex lithology, if the soil is dominated by sand and is cemented by ice (i.e. contains $\geq 3\text{--}4 \text{ wt}\%$ water [43]), ice grains

will bear the brunt of any tensile load, and frozen soil will deform by the same mechanisms that polycrystalline ice does, albeit at different rates [44].

Polycrystalline ice deforms by dislocation creep, grain boundary sliding, diffusional flow, recrystallization and microcracking, where each mechanism can be described by some form of power-law relation similar to Eq. 7 (e.g. [41,45–49]). At steady-state stresses of ≥ 1 MPa, the creep of polycrystalline ice is dislocation climb-limited, independent of grain size, and characterized by a stress exponent n of 4 (Table 1) ([49], and references therein). At lower steady-state stresses ($0.1 < \sigma < 5$ MPa) and strain rates ($10^{-9} < \dot{\epsilon}^n < 10^{-6} \text{ s}^{-1}$), grain boundary sliding-accommodated basal slip (GBS) is the dominant creep mechanism [49]. GBS is characterized by a stress exponent of 1.8 and is strongly grain-size dependent, with $A_0 = A'_0 d^{-p}$, where d is the grain size in meters and $p = 1.4$ is the grain size exponent (Table 1).

Assuming that ice grains in ice-undersaturated sand will grow into existing pore spaces and be of the same length scale as the sand grains themselves (0.1–1 mm diameter), either dislocation creep or GBS could be a viable creep mechanism for the range of stresses (≤ 2 MPa), strain rates (10^{-6} s^{-1}), and total strains (~ 0.01) appropriate to this study (figures 2a and 3a in [4]). Larger ice grain sizes will tend to favor climb-limited creep. Both creep mechanisms suggest effective viscosities for pure ice between 10^{13} and 10^{15} Pa s for $1 < \sigma < 2$ MPa and $223 \leq T \leq 258 \text{ K}$ (Fig. 6).

Some question remains as to whether steady-state deformation would ever be achieved in ice exposed to diurnal load cycles (although grain size sensitive creep in polycrystalline ice of grain size ≤ 0.1 mm may reach steady state after strains of

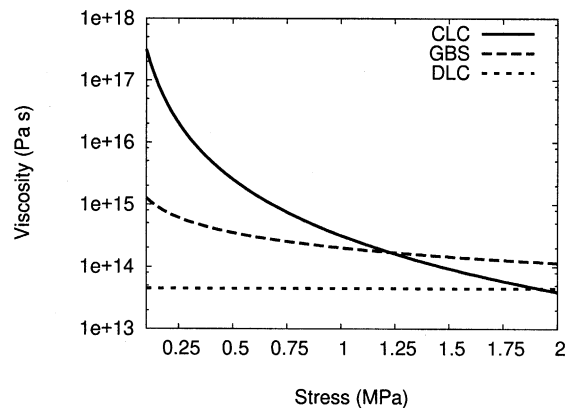


Fig. 6. Effective viscosity of ice deforming by dislocation climb-limited steady-state creep *CLC* (solid), grain boundary sliding-accommodated basal slip-limited steady-state creep *GBS* (dashed) and drag-limited transient creep *DLC* (dotted). An ice grain size, d , of 0.2 mm is used to represent fine-grained ice grown in the pore space of a compacted sand.

only ~ 0.01). In experiments that consider transient stresses of 0.1–3.0 MPa, there is not sufficient energy to initiate new dislocations, creep is limited by drag on existing dislocations, and the stress exponent is 1.0 (Table 1) [50,51]. We suggest a scenario in which, during the maximum strain rate portion of the first load cycle, dislocation density increases with increasing stress, and ice deforms by climb-limited power-law creep (and/or GBS). After the first load cycle, if the time scale of recovery is long compared to the time scale of loading, the dislocation density will remain constant at the density achieved during the maximum strain-rate portion of the cycle [51]. Cole and Durall [51] found evidence for 7–25% recovery in sea ice after 1–3 days under no stress at 268 K. Therefore, in the absence of experimental data, we estimate that recovery over 11 h at 263–223 K would be negligible.

Table 1
Viscosity parameters of ice

Creep law	$T \leq 258 \text{ K}$				$T > 258 \text{ K}$			
	A'_0 [$\text{Pa}^{-n} \text{ s}^{-n} \text{ m}^p$]	Q [J/mol]	n	p	A'_0	Q	n	p
Climb-limited[49]	4.0×10^{-19}	6.0×10^4	4	0	6.0×10^4	1.8×10^5	4	0
GBS-limited[49]	6.2×10^{-14}	4.9×10^4	1.8	1.4	4.8×10^{15}	1.9×10^5	1.8	1.4
Drag-limited[51]	1.7×10^{-2}	5.3×10^4	1	0	1.7×10^{-2}	5.3×10^4	1	0

We can determine A'_0 (which is dependent on dislocation density, (e.g. [47,51])) for drag-limited creep in pure ice as follows. The maximum strain rate at 268 K and 2 MPa should be the same during the first load cycle and all subsequent load cycles. Climb-limited creep at 268 K and 2 MPa yields $\dot{\epsilon}^n = 8.1 \times 10^{-7} \text{ s}^{-1}$, the maximum strain rate achieved during the first load cycle. In order for $\dot{\epsilon}^n = 8.1 \times 10^{-7} \text{ s}^{-1}$ to be achieved by drag-limited creep during subsequent load cycles, A'_0 must be $1.7 \times 10^{-2} \text{ Pa}^{-1} \text{ s}^{-1}$ [51] (Table 1). After the first load cycle, the effective viscosity of pure ice deforming by drag-limited creep at 1–2 MPa and 258–223 K ranges from 10^{13} to 10^{14} Pa s (Fig. 6).

Importantly, the inclusion of dispersed coarse particulates (e.g. sand) in ice likely limits flaw lengths and terminates glide planes, significantly reducing creep rates. Durham et al. [52] observed that for ice-saturated quartz sand at 223 K, the effective viscosity increases by two orders of magnitude. Similarly, Hooke et al. [53] found that ice with 35% fine sand at 263 K deformed at 5% of the experimental creep rate for pure ice at the same temperature. Thus, we expect frozen soils to have minimum effective viscosities on the order of 10^{14} to 10^{16} Pa s .

We see that the range of possible soil viscosities straddles the critical viscosity for cracking of $1.8 \times 10^{14} \text{ Pa s}$ that was determined analytically in Section 3. The fact that frozen soil viscosity lies very close to this transition zone may explain why Neoproterozoic sand wedges are not ubiquitous but occur in favorable thermal regimes and soil rheologies.

4.2. Elastic parameters

Measured values of Poisson's ratio, ν , for frozen soils between 250 and 273 K range between 0.12 and 0.45 [54,55]. The absolute value of and variance in ν tend to decrease at lower temperatures, in drier regimes, and in coarser soils where liquid water is less abundant along grain boundaries. Although it is likely that smaller ν may have led to larger elastic stresses, we consider a ν of 0.3 to give a lower bound to accumulated elastic stresses.

Gold [56] found that, for ice above 233 K, Young's modulus obeys the equation $E = (2.339 \times 10^{10} \text{ Pa}) - (6.48 \times 10^7 \text{ Pa K}^{-1})T$. Coarse-grained frozen soils with little or no unfrozen water have E values up to five times higher than ice, while fine-grained frozen soils have E values similar to ice [54]. We note that the uncertainty in the value for E is an order of magnitude greater than the expected variation of E with temperature. Therefore, we ignore any temperature dependence and adopt $E = 10^{10} \text{ Pa}$ to give a minimum estimate of elastic stress build-up in the frozen soil.

4.3. Thermal expansivity

Hobbs [57] reviewed measurements of the coefficient of thermal expansion of ice, α , and found that for $150 \leq T \leq 273 \text{ K}$, $\alpha = (2.47 \times 10^{-7} \text{ K}^{-2})T - (1.17 \times 10^{-5} \text{ K}^{-1})$. Most silicate rocks have thermal expansivities two to ten times lower than ice; therefore, Mellon [22] considered a linear mixture of 55% basalt and 45% ice to deduce the relation $\alpha = (1.11 \times 10^{-7} \text{ K}^{-2})T - (1.42 \times 10^{-6} \text{ K}^{-1})$ for frozen soil on Mars. However, composite mixtures often behave very differently than their individual components (e.g. [58]). Bourbonnais and Ladanyi [59] measured α values of $\sim 2.5 \times 10^{-5} \text{ K}^{-1}$ for frozen sand in the laboratory, with α decreasing slightly with temperature. Mackay [60] studied crack widths in areas of active ice wedge growth and determined an α for heterogeneous frozen silt of $20\text{--}40 \times 10^{-5} \text{ K}^{-1}$, or about 10 times the values considered by Mellon [22] and Bourbonnais and Ladanyi [59] and at least two times greater than any experimentally derived α_{ice} . We apply a constant $\alpha = 2.3 \times 10^{-5} \text{ K}^{-1}$ as a conservative estimate of the coefficient of thermal expansion.

4.4. Fracture toughness

The fracture toughness, K_{IC} , of pure ice varies from 0.05 to 0.15 $\text{MPa m}^{1/2}$ [61,62], while the K_{IC} of concrete, silica, and most rock is between 0.75 and 1.5 $\text{MPa m}^{1/2}$ [40]. Konrad and Cummings [63] performed experiments on frozen soils beneath asphalt at 268 K which indicated that the

fracture toughness of frozen sand increases from 0.04 to 0.70 MPa m^{1/2} when the weight percent of ice increases from ~3 to ~10%. Similar tests conducted by Li and Yang [64] on silty sand at 263 K showed K_{IC} increasing from 0.13 to 0.83 MPa m^{1/2} when the weight percent of ice increases from ~5 to ~7.5%. Within the range of values listed above, the fracture toughness of frozen soil decreases with increasing temperature [64], decreasing load rate [64] and decreasing grain size of soil particles [63]. When the weight percent of ice is greater than about 8%, there is some evidence that K_{IC} begins to decrease as ice content increases and behaves more like pure ice [64]. For frozen sand at temperatures ≤ 258 K, we consider $0.1 < K_{IC} < 0.8$.

5. Numerical results

5.1. Method

We develop a numerical model to evaluate the effects of more complicated temperature- and stress-dependent rheologies. The problem at each time step is broken into three parts. First, we calculate the one-dimensional thermal profile, $T(z)$, at depth intervals Δx using Eq. 2. Second, we calculate the stress, $\sigma(z)$, using Eq. 10. Third, we integrate Eq. 12 to find the crack edge stress intensity factor, $K(b)$, for the full range of crack lengths, b . The equation for stress is integrated forward in time from an initially unstressed state using a fourth-order Runge–Kutta method. We run the code for long enough to remove the transients and then output the values of T , σ , and K for the time t_{\max} at which the potential crack depth is maximized (the exact value of t_{\max} depends on the specific rheology used and is determined by visual inspection of the results).

This code has been benchmarked against the analytical results derived earlier for a constant viscosity, as shown in Fig. 3.

5.2. Results

Fig. 7 shows the results of the numerical experiments (see the figure caption for details). The top

row of graphs (Fig. 7a,b) shows σ and K assuming constant viscosities of 10^{13} – 10^{16} Pa s for reference. These calculations are equivalent to the analytical results derived above.

For the stress- and temperature-dependent rheologies of the other subfigures, we show three different rheologies in each pair. The curves marked ice assume a pure ice rheology as summarized in Table 1. The curves marked soil1 and soil2 employ viscosities in which A_0 is decreased by a factor of 10 and 100, respectively, to approximate the behavior of sand/ice mixtures (see Section 4.1 for discussion).

For the the bottom row (Fig. 7g,h), we assume a temperature-dependent rheology. Although the results are very similar to the constant viscosity case, the temperature dependence of viscosity tends to amplify stresses above the skin depth during the cold part of the day and reduce stresses above the skin depth during the warm part of the day.

Fig. 7e,f and c,d show the results of stress- and temperature-dependent calculations, with $n = 1.8$ and 4, respectively. In these cases, particularly with $n = 4$, the stress dependence of viscosity strongly limits the accumulated stress near the surface and changes t_{\max} . The shape of the $K(b)$ curve is more complicated than in the Newtonian cases; see the following section for more discussion of this behavior.

In all cases, we predict that the sand/ice mixtures will exhibit cracks of depths ≥ 0.5 m.

6. Discussion

The key insight here is that the depth to which a fracture propagates in permafrost depends more on the material properties of the ground than on the penetration depth of surface temperature waves. For example, consider a cold event that reaches a depth z_ω and develops a stressed layer of thickness z_ω . If the ground below is cold and brittle, cracks will initiate in the stressed layer and propagate to depths, b , many times the thickness of z_ω . However, if conditions are similar to those found in high latitudes today, where ground temperatures increase with depth during the winter as

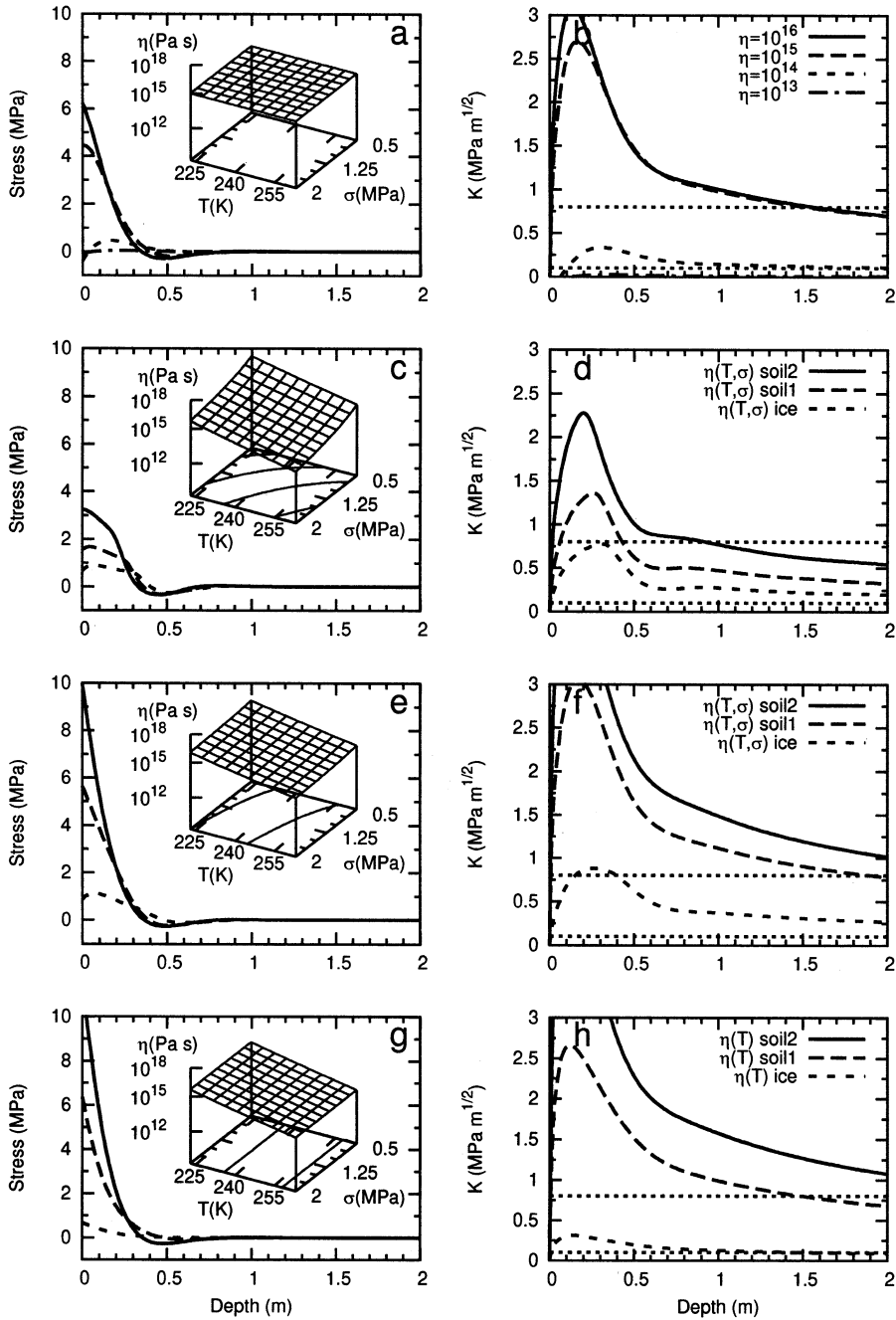


Fig. 7. Numerical calculations of stress (a,c,e,g) and intensity factor (b,d,f,h) distribution with depth for various viscosity laws appropriate for ice and frozen soil (see text). (a,b) are calculated assuming linear viscosity, (c,d) are calculated assuming climb-limited creep, (e,f) are calculated assuming GBS-limited creep with 0.2 mm diameter ice grains, and (g,h) are calculated assuming drag-limited creep. In (b,d,f,h), horizontal dashed lines at $K=0.1$ and 0.8 $\text{MPa m}^{1/2}$ indicate the possible range of K_{IC} for frozen soil. Insets in (a,c,e,g) show how the viscosity of soil1 varies with temperature and stress (viscosity parameters taken from Table 1). All calculations assume $\kappa=10^{-6}$ m/s^2 , $\alpha(600 \text{ Ma})=7.97 \times 10^{-5}$ s^{-1} , $\Delta T=20$ K, $T_{\text{avg}}=243$ K, $E=10$ GPa, $\nu=0.3$, $\alpha=2.3 \times 10^{-5}$ K^{-1} , $\rho_{\text{ice}}=900$ kg m^{-3} and $\rho_{\text{soil}}=2500$ kg m^{-3} .

a memory function of the previous summer's warmth [65], cracks initiated within the stressed layer will be arrested in the warmer, more viscous ground below. Therefore, high-latitude Quaternary sand/ice wedges often form on the same length scale as the diffusion of cold events through the ground because the un-cooled ground below is not brittle. Conversely, during a snowball Earth interval, the ground is dry and cold year-round. The large stresses associated with diurnal temperature variations, though only felt in the upper 16 cm of the ground, are more than enough to propagate fractures ≥ 0.5 m deep through the brittle ground below.

The two largest unknowns that could lead to significant errors in our calculations are the rheology and the fracture toughness of frozen ground. We saw in Section 3 that the details of viscous creep were not crucially important and that as long as we could constrain the effective viscosity of frozen soil to be $\geq 1.8 \times 10^{14}$ Pa s, cracks would form. As observed and predicted effective viscosities for ice [41,66] and frozen sand [52,53,67,68] appear to range between 10^{13} and 10^{16} Pa s, it is likely that some permafrost is vulnerable to cracking while some is not.

The second important unknown in these calculations is the fracture toughness, K_{IC} , which varies across almost an order of magnitude depending on ice content and soil grain size, and to a lesser extent on temperature and load rate. However, considering the full range of possible K_{IC} in frozen ground, we conclude that when cracks occur, they can reach depths of at least 50 cm.

As we stated in Section 3.1, the stresses in the soil near the surface will never exceed the tensile strength of the soil; when this stress is reached, the soil will fracture and a crack will initiate. One could make the argument, therefore, that σ_θ in Eq. 26 should be ≤ 2 MPa, the maximum tensile strength of frozen ground [54,55,65]. This statement is true if we model only the strain energy available to the crack during initial rupture. However, if the ground continues to contract thermally after initial rupture, the stresses that would have been near the surface directly above the crack of depth b are either (1) focused at depth in the crack tip leading to further crack propagation;

and/or (2) used to form new cracks at a horizontal distance less than the distance, y , at which stress relief owing to crack formation is < 10 –20% ($y \sim 2b$; [65,69]). At horizontal distances greater than $2b$, we consider the ground to be part of a different micro-system, which does not experience significant stress relief from the propagation of the initial crack.

The most accurate model of crack propagation would allow neighboring cracks at $y < 2b$ to form and grow. A variety of experimental and theoretical investigations show that, as parallel thermal contraction cracks grow, they will tend to interact with each other unstably so that some cracks stop growing while others extend at a faster rate [69–71]. In a material with no initial flaws, neighboring micro-cracks can pirate as much as 25% of the available strain energy, although the system is still characterized by a collection of long cracks separated horizontally by a distance $y \sim 2b$ [70]. However, in a material that contains even a very small number of imperfections, little or no strain energy will be spent opening and closing minor cracks and nearly all of the available strain energy will be used to propagate long cracks to depths b at a distance $\sim 2b$ apart [69–71]. Because permafrost

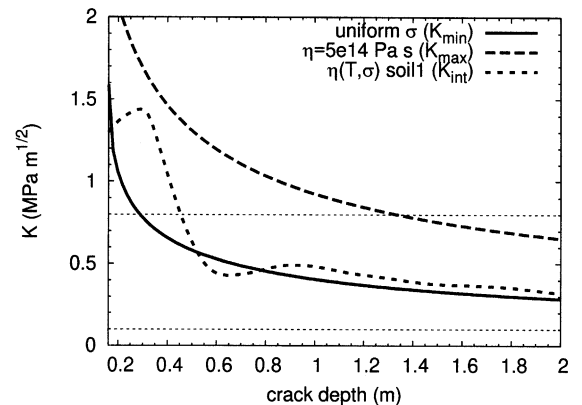


Fig. 8. Intensity factor versus depth calculated (solid) using Eq. 13 for a stress $\sigma = 2$ MPa applied uniformly from $z = 0$ to $z = z_\omega$; (dashed) using Eq. 12 for a variable stress (Eq. 20) and linear viscosity $\eta = 10^{15}$ Pa s; and (dotted) stress- and temperature-dependent viscosity for soil1 (see Fig. 7d). Note that the plot begins at the skin depth $z_\omega = 0.16$ m. Horizontal dashed lines at $K = 0.1$ and 0.8 MPa $m^{1/2}$ indicate the possible range of K_{IC} for frozen soil.

is an imperfect material with abundant flaws, most of the strain energy available during a cycle of cooling and thermal contraction will be used to propagate a single fracture. We model pre-crack stress and ignore the tensile strength of the material, allowing the stresses to exceed 2 MPa so that the total available strain energy will be used to extend a single crack.

It is beyond the scope of this paper to model interactions between cracks. Instead, we present lower and upper bounds on potential crack depth (Fig. 8). Minimum crack depths will be achieved if we assume a uniform stress of 2 MPa through the skin depth. We see that when the effects of stress-dependent rheology are considered, stresses exceeding 2 MPa in the surface layers will over-predict the degree of viscous relaxation, thus leading to stress intensity values nearly identical to those of the uniform 2 MPa stress example. For non-stress-dependent rheologies with viscosities $\geq 1.8 \times 10^{14}$ Pa s, allowing stresses in the upper centimeters of soil to exceed the tensile strength of permafrost by a factor of 2–5 predicts cracks one to four times longer than the uniform 2 MPa case, thus placing an upper bound on crack depth (Fig. 8). Crack depths likely approach this upper bound when few if any minor cracks grow around the dominant rupture after initial failure. To quantify how much strain energy is squandered on microcracking around the major fracture, detailed experiments like those of Mackay and Burn [18] must be conducted to observe exactly how cracks form and grow in permafrost during the passage of a cold wave.

At least two potential tests of our model for thermal contraction cracking could be conducted. First and simplest, cold room experiments on blocks of frozen sand subject to rapid cyclic temperature variations could determine potential crack depths experimentally. Second, high-resolution imaging of moderate altitude plateaus on the Martian equator, where diurnal temperature variations exceed 60°C, temperatures rarely rise above 5°C [37], and ground ice is prevalent [23], should reveal active ground cracking. However, equatorial Martian sand wedges may prove very difficult to image, as low solar-incidence angles at the equator hinder the imaging of low-relief land

features with conventional passive recorders. Furthermore, it would have to be demonstrated that the equatorial wedges were very recent and not formed during a Martian high-obliquity episode [72].

7. Conclusions

To investigate whether stresses associated with the diurnal temperature cycle during a snowball Earth event could have been responsible for sand-wedge growth, we present a quantitative analysis of the process of crack formation in solids subject to periodic temperature variations. We derive analytical expressions relating the Newtonian viscosity to the potential crack depth, concluding that cracks will form only in frozen soils with viscosities greater than 10^{14} Pa s. We also show numerical calculations of crack growth in frozen soils with more complicated material properties, such as a stress- and temperature-dependent rheology, and conclude that a linearized viscosity law leads to accurate predictions of crack depth. We also conclude that during cyclic loading, if the time scale of recovery is long compared to the time scale of loading, dislocation density will likely remain constant and the non-linear process of dislocation multiplication will be inactive, leaving a linear stress–strain rate relationship. Therefore, a linear viscosity law may be the most accurate characterization of frozen soil behavior exposed to a diurnal temperature forcing.

Even when using conservative estimates for all material parameters, we find that effective viscosities for frozen ground likely vary from 10^{14} to 10^{16} Pa s. We expect that temperature regimes and soil rheologies favorable for crack formation would have been common at the equator during a snowball Earth episode. Furthermore, we find that temperature variations on the order of tens of degrees over 11–24 h periods yield cracks one-half to several meters deep, similar to the length scale of sand wedges seen in the geologic record. High degrees of seasonality would not have been necessary to form sand-wedge polygons at the equator during a snowball Earth.

Acknowledgements

The authors benefited greatly from discussions with Thorsten Becker, David Cole, Brian Evans, David Evans, Bernard Hallet, Paul Hoffman, Peter Moore, Richard O'Connell, Lawrence Plug, Cin-Ty Lee, James Rice, Erland Schulson, and John Shaw. Two anonymous reviews improved the text substantially. The research was funded by the NASA Astrobiology Institute and NSF. [RV]

References

- [1] G. Williams, Late precambrian glacial climate and the Earth's obliquity, *Geol. Mag.* 112 (1975) 441–465.
- [2] G. Williams, History of the Earth's obliquity, *Earth Sci. Rev.* 34 (1993) 1–45.
- [3] G. Williams, The paradox of Proterozoic glaciation at sea level and strong seasonality near the paleoequator: Evidence and implications, *Geol. Soc. Aust. Abstracts* 65 (2001) 108–112.
- [4] J. Kirschvink, Late Proterozoic low-latitude glaciation: The snowball earth, in: J. Schopf, C. Klein (Eds.), *The Proterozoic Biosphere*, Cambridge University Press, 1992, pp. 51–52.
- [5] P. Hoffman, A. Kaufman, G. Halverson, D. Schrag, A Neoproterozoic snowball Earth, *Science* 281 (1998) 1342–1346.
- [6] P. Hoffman, D. Schrag, The snowball Earth hypothesis testing the limits of global change, *Terra Nova* 14 (2002) 129–155.
- [7] G. Williams, Sedimentology, stable-isotope geochemistry and palaeoenvironment of dolostones capping late Precambrian glacial sequences in Australia, *J. Geol. Soc. Aust.* 26 (1979) 377–386.
- [8] I. Fairchild, Balmy shores and icy wastes: the paradox of carbonates associated with glacial deposits in Neoproterozoic times, *Sediment. Rev.* 1 (1993) 1–16.
- [9] M. Kennedy, Stratigraphy, sedimentology, and isotopic geochemistry of Australian Neoproterozoic postglacial cap dolostones: Deglaciation, $\delta^{13}\text{C}$ excursions, and carbonate precipitation, *J. Sediment. Res.* 66 (1996) 1050–1064.
- [10] J. Grotzinger, N. James, Precambrian carbonates: Evolution of understanding, in: J. Grotzinger, N. James (Eds.), *Carbonate Sedimentation and Diagenesis in the Evolving Precambrian World*, Spec. Pub. 67, SEPM, 2000.
- [11] N. Evans, L. Rossbacher, The last picture show: Small-scale patterned ground in Lunae Planum, Reports of the Planetary Geology Program - 1980, NASA Tech. Memo TM 82385 (1980) 376–378.
- [12] G. Brook, Ice wedge polygons, baydjarakhs, and alases in Lunae Planum and Chrs Planitia, Mars, Reports of the Planetary Geology Program - 1982, NASA Tech. Memo. TM 85127 (1982) 265–267.
- [13] B. Luchitta, Permafrost on Mars: Polygonally fractured ground, Permafrost, 4th International Conference Proceedings, 1983.
- [14] N. Siebert, J. Kargel, Small-scale Martian polygonal terrain: Implications for liquid surface water, *Geophys. Res. Lett.* 28 (2001) 899–902.
- [15] E. de K. Leffingwell, Ground-ice wedges: The dominant form of ground-ice on the north coast of Alaska, *J. Geol.* 23 (1915) 635–654.
- [16] R. Black, Periglacial features indicative of permafrost: ice and soil wedges, *Quat. Res.* 6 (1976) 3–26.
- [17] J. Mackay, Air temperature, snow cover, creep of frozen ground, and the time of ice-wedge cracking, western Arctic coast, *Can. J. Earth Sci.* 30 (1993) 1720–1729.
- [18] J. Mackay, C. Burn, The first 20 years (1978–1979 to 1998–1999) of ice wedge growth at the Illisarvik experimental drained lake site, western Arctic coast, Canada, *Can. J. Earth Sci.* 39 (2002) 95–111.
- [19] J. Mackay, Ice-wedge cracks, Garry Island, Northwest Territories, *Can. J. Earth Sci.* 11 (1974) 1366–1383.
- [20] R. Black, Patterned - ground studies in Victoria Land, *Ant. J. USA* 17 (1982) 53–54.
- [21] C. Downie, P. Wilkinson, *The Geology of Kilimanjaro*, Dept. Geol., Univ. Sheffield, 1972.
- [22] M. Mellon, Small-scale polygonal features on Mars: Seasonal thermal contraction cracks in permafrost, *J. Geophys. Res.* 102 (1997) 25617–25628.
- [23] P. Lanagan, A. McEwen, L. Keszthelyi, T. Thordarson, Rootless cones on Mars indicating the presence of shallow equatorial ground ice in recent times, *Geophys. Res. Lett.* 28 (2001) 2365–2367.
- [24] G. Williams, D. Tonkin, Periglacial structures and palaeoclimatic significance of a late Precambrian block field in the Cattle Grid copper mine, Mount Gunson, South Australia, *Aust. J. Earth Sci.* 32 (1985) 287–300.
- [25] M. Deynoux, Periglacial polygonal structures and sand wedges in the late Precambrian glacial formations of the Taoudeni Basin in Adrar of Mauretania (West Africa), *Palaeogeogr. Palaeoclimatol. Palaeoecol.* 39 (1982) 55–70.
- [26] N. Chumakov, Late Precambrian glaciation of Spitsbergen, *Dokl. Akad. Nauk USSR, Earth Sci. Sect.* 180 (1968) 115–118.
- [27] M. Edwards, Glacial retreat sedimentation in the Smalfjord Formation, late Precambrian, North Norway, *Sedimentology* 22 (1975) 75–94.
- [28] J. Nystuen, Late Precambrian Moelv tillite deposited on a discontinuity surface associated with a fossil ice wedge, Rendalen, southern Norway, *Norsk Geol. Tidsskr.* 56 (1976) 29–50.
- [29] A. Spencer, Late Precambrian glaciation in Scotland, *Geol. Soc. London Mem.* 6 (1971) 100.
- [30] P. Schmidt, G. Williams, The Neoproterozoic climatic paradox: Equatorial palaeolatitude for Marinoan glaciation near sea level in South Australia, *Earth Planet. Sci. Lett.* 104 (1995) 347–357.

- [31] L. Sohl, N. Christie-Blick, D. Kent, Paleomagnetic polarity reversals in Marinoan (ca. 600 Ma) glacial deposits of Australia: Implications for the duration of low-latitude glaciation in Neoproterozoic time, *Geol. Soc. Am. Bull.* 111 (1999) 1120–1139.
- [32] D. Evans, Stratigraphic, geochronological and paleomagnetic constraints upon the Neoproterozoic climatic paradox, *Am. J. Sci.* 300 (2000) 347–433.
- [33] R. Wetherald, S. Manabe, The effects of changing the solar constant on the climate of a general circulation model, *J. Atmos. Sci.* 32 (1975) 2044–2059.
- [34] J. Walker, Strange weather on Snowball Earth, *Earth Systems Processes Meeting*, Edinburgh, Scotland, *Progr. Abs.*, *Geol. Soc. Am.*, 2001, p. 110.
- [35] G. Williams, Late Precambrian tidal rhythmites in South Australia and the history of the Earth's rotation, *J. Geol.* 146 (1989) 97–111.
- [36] G. Williams, Precambrian tidal and glacial clastic deposits implications for Precambrian Earth - Moon dynamics and palaeoclimate, *Sediment. Geol.* 120 (1998) 55–74.
- [37] C. Leovy, Weather and climate on Mars, *Nature* 412 (2001) 245–249.
- [38] D.J. Turcotte, G. Schubert, *Geodynamics*, Wiley, 1982.
- [39] A. Lachenbruch, Depth and spacing of tension cracks, *J. Geophys. Res.* 66 (1961) 4273–4292.
- [40] B. Lawn, *Fracture of Brittle Solids*, Cambridge University Press, 1993.
- [41] D. Goldsby, D. Kohlstedt, R. Pappalardo, A composite flow law for water ice for use in modelling of glaciers, polar caps, and icy planetary interiors, *Proceedings, Lunar and Planetary Science XXXII*, 2001, p. 2067.
- [42] F.A. Dahlen, J. Tromp, *Theoretical Global Seismology*, Princeton University Press, 1998.
- [43] R. Black, Growth of patterned ground in Victoria Land, Antarctica, 2nd Permafrost Int. Conf., Yakutsk, *Natl. Res. Council Publ.* 2115, 1973, pp. 193–203.
- [44] O. Andersland, B. Ladanyi, *An Introduction to Frozen Ground*, Chapman and Hall, 1994.
- [45] L. Gold, The process of failure of columnar-grained ice, *Philos. Mag.* 26 (1972) 311–328.
- [46] D. Homer, J. Glen, The creep activation energies of ice, *J. Glaciol.* 21 (1978) 429–444.
- [47] J. Weertman, Creep deformation of ice, *Annu. Rev. Earth Planet. Sci.* 11 (1983) 215–240.
- [48] A. Elvin, S. Sunder, Microcracking due to grain boundary sliding in polycrystalline ice under uniaxial compression, *Acta Mater.* 44 (1996) 43–56.
- [49] D. Goldsby, D. Kohlstedt, Superplastic flow of ice: Experimental observations, *J. Geophys. Res.* 106 (2001) 11017–11030.
- [50] T. Langdon, Creep mechanisms in ice, *Symposium on the Physics and Chemistry of Ice*, 1973, pp. 356–361.
- [51] D. Cole, G. Durell, A dislocation-based analysis of strain history effects in ice, *Philos. Mag.* A 81 (2001) 1849–1872.
- [52] W. Durham, S. Kirby, L. Stern, Effects of dispersed particulates on the rheology of water ice at planetary conditions, *J. Geophys. Res.* 97 (1992) 20883–20897.
- [53] R. Hooke, B. Dahlen, M. Kauper, Creep of ice containing dispersed fine sand, *J. Glaciol.* 11 (1972) 327–336.
- [54] C. Kaplar, Laboratory determination of the dynamic moduli of frozen soils and of ice, *Proceedings, Permafrost International Conference Publ.* 1287, 1963, pp. 293–301.
- [55] N. Tsytovich, *The Mechanics of Frozen Ground*, McGraw-Hill, 1975.
- [56] L. Gold, Some observations on the dependence of strain on stress for ice, *Can. J. Phys.* 36 (1958) 1265–1275.
- [57] Hobbs, *Ice Physics*, Oxford University Press, 1974.
- [58] A. Brannert, *Cement-based Composites*, E and FN Spon, 1995.
- [59] J. Bourbonnais, B. Ladanyi, The mechanical behavior of frozen sand down to cryogenic temperatures, *Fourth International Symposium on Ground Freezing*, 1985.
- [60] J. Mackay, The first 7 years (1978–1985) of ice wedge growth, Illisarvik experimental drained lake site, western Arctic coast, *Can. J. Earth Sci.* 23 (1986) 1782–1795.
- [61] M. Rist, P. Sammonds, S. Murrell, P. Meredith, C. Doake, H. Oerter, K. Matsuki, Experimental and theoretical fracture mechanics applied to Antarctic ice fracture and surface crevassing, *J. Geophys. Res.* 104 (1999) 2973–2987.
- [62] W. Nixon, E. Schulson, A micromechanical view of the fracture toughness of ice, *J. Phys. Coll. C1* 48 (1987) 313–319.
- [63] J. Konrad, J. Cummings, Fracture toughness of frozen base and subbase soils in pavement, *Can. Geotech. J.* 38 (2001) 967–981.
- [64] H. Li, H. Yang, Experimental investigations of fracture toughness of frozen soils, *J. Cold Regions Eng.* 14 (2000) 43–49.
- [65] A. Lachenbruch, Mechanics of thermal contraction cracks and ice-wedge polygons in permafrost, *Spec. Pap. Geol. Soc. Am.* 70 (1962) 69.
- [66] W. Durham, L. Stern, Rheological properties of water ice applications to satellites of the outer planets, *Annu. Rev. Earth Planet. Sci.* 29 (2001) 295–330.
- [67] F. Sayles, Triaxial and creep tests on frozen Ottawa sand, *Proc. 2nd Permafrost Int. Conf.*, Yakutsk, *Natl. Res. Council Publ.* 2115, 1973.
- [68] J. Ting, The creep of frozen sands: Qualitative and quantitative models, *MIT Dept. of Civil Engineering Thesis*, 1981.
- [69] Z.P. Bazant, H. Ohtsubo, K. Aoh, Stability and post-critical growth of a system of cooling or shrinkage cracks, *Int. J. Fractures* 15 (1979) 443–456.
- [70] J. Geyer, S. Nemat-Nasser, Experimental investigation of thermally induced interacting cracks in brittle solids, *Int. J. Solids Struct.* 18 (1982) 349–356.
- [71] S. Nemat-Nasser, Y. Sumi, L. Keer, Unstable growth of tension cracks in brittle solids: Stable and unstable bifurcations, snap through, and imperfection sensitivity, *Int. J. Solids Struct.* 16 (1980) 1017–1035.
- [72] F. Costard, F. Forget, N. Mangold, J. Peulvast, Formation of recent Martian debris flows by melting of near-surface ground ice at high obliquity, *Science* 295 (2002) 110–113.